

Article

A Tunable Gain and Bandwidth Low-Noise Amplifier with 1.44 NEF for EMG and EOG Biopotential Signal

Rafael Vieira ^{1,2,*}, Fabian Näf ^{2,3} , Ricardo Martins ^{1,2} , Nuno Horta ^{1,2}, Nuno Lourenço ^{1,*} 
and Ricardo Póvoa ^{1,4}

¹ Instituto de Telecomunicações, 1049-001 Lisboa, Portugal; ricmartins@lx.it.pt (R.M.); nuno.horta@lx.it.pt (N.H.); rpvoa@lx.it.pt (R.P.)

² Instituto Superior Técnico, Universidade de Lisboa, 1049-001 Lisboa, Portugal; fabian.naf@tecnico.ulisboa.pt

³ Instituto de Engenharia de Sistemas e Computadores-Investigação e Desenvolvimento (INESC-ID), 1000-029 Lisboa, Portugal

⁴ Escola Superior Náutica Infante D. Henrique, 2770-058 Oeiras, Portugal

* Correspondence: rafael.a.vieira@tecnico.ulisboa.pt (R.V.); nlourenco@lx.it.pt (N.L.)

Abstract: This paper presents a low-noise inverter-based current-mode instrumentation amplifier with tunable gain and bandwidth for electromyogram (EMG) and electrooculogram (EOG) biopotential signals, targeting low input noise while maintaining low power consumption. The gain tuning method is based on pseudo-resistors, whereas the bandwidth is tunable due to a varactor system that is controlled by the same control voltage that tunes the gain. The circuit was designed and manufactured using the 110 nm UMC CMOS technology node, occupying an area of 0.624 mm². The circuit presents a functioning mode for each biopotential signal with different characteristics, for the EMG a gain of 34.7 dB and a bandwidth of 1412 Hz was measured, with an input referred noise of 1.407 μ V which matches a noise efficiency factor of 1.44. The EOG mode achieves a 39.5 dB gain and a 22.4 Hz bandwidth while presenting an input-referred noise of 0.829 μ V corresponding to a noise efficiency factor of 6.37. For both modes, the supply voltage is 1.2 V and the circuit consumes 1 μ A.

Keywords: low-noise amplifier; low power; tunable gain; tunable bandwidth; biopotential signals; CMOS



Citation: Vieira, R.; Näf, F.; Martins, R.; Horta, N.; Lourenço, N.; Póvoa, R. A Tunable Gain and Bandwidth Low-Noise Amplifier with 1.44 NEF for EMG and EOG Biopotential Signal. *Electronics* **2023**, *12*, 2592. <https://doi.org/10.3390/electronics12122592>

Academic Editor: Kiat Seng Yeo

Received: 25 April 2023

Revised: 24 May 2023

Accepted: 2 June 2023

Published: 8 June 2023



Copyright: © 2023 by the authors. Licensee MDPI, Basel, Switzerland. This article is an open access article distributed under the terms and conditions of the Creative Commons Attribution (CC BY) license (<https://creativecommons.org/licenses/by/4.0/>).

1. Introduction

Low-power wearable and implantable devices for long-term continuous monitoring of biopotential signals have been an important research topic with the prospect that they can improve people's everyday life [1]. In recent years, these monitoring devices have seen significant advancements, bringing the concept of a wireless body area network (WBAN) [2]. WBANs are composed of several sensors connected through a network being able to detect and record biopotential signals to detect diseases and monitor the patient's health. Table 1 presents the amplitude and frequency range characteristics of some common biopotential signals that can be recorded to detect diseases and monitor the patient's health [3]. Low-power analog front-ends (AFEs) are used in the acquisition of such biopotential signals, which must comply with some sets of complex challenges, such as detecting the feeble biopotential signal while introducing minimum noise to the already weak signal for proper recording [4] and providing high linearity [5]. Moreover, portable AFEs have even more restrictions since they have very limited current budgets and, therefore, they have low power consumption to extend the operation lifetime while presenting small form factors to be ergonomic and, hence, fully benefiting from dedicated integrated circuit solutions. The AFEs usually consist of four blocks: a low-noise amplifier (LNA), a filtering block, a variable-gain amplifier, and an analog-to-digital converter, as shown in Figure 1, with the LNA being typically one of the most power-hungry blocks to reduce the noise introduced

in the system. Yet, there are some AFEs that are used only for signal detection, normally presenting lower power consumptions with less constraint on the noise requirements [6,7].

Table 1. Characteristics of biopotential signals.

Characteristics	Amplitude (mV)	Frequency Range (Hz)
Electrocardiogram (ECG)	1–5	0.05–100
Electroencephalogram (EEG)	0.001–0.01	0.5–40
Electromyogram (EMG)	1–10	20–2000
Electrooculogram (EOG)	0.01–0.1	dc–10

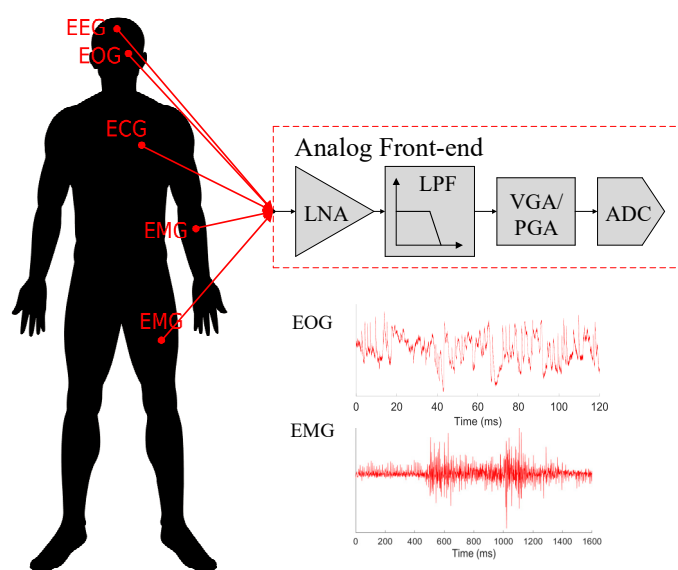


Figure 1. Example of a biopotential acquisition system block diagram.

This paper presents a low-power LNA for fully recording electromyogram (EMG) and electrooculogram (EOG) biopotential signals. This low-power LNA focuses on enabling two working modes with gain and cutoff frequencies that can be tuned for each biopotential signal. Moreover, the circuit has enough reconfigurability to achieve other gains and a wider range of cutoff frequencies.

The EMG signal has a maximum frequency range of 2000 Hz; the cutoff frequency respective to this mode should be around this value. This mode will be, from now on, mentioned as high cutoff frequency (HCF) mode. Analogously, the mode concerning the EOG signal is designated the low cutoff frequency (LCF). The LCF presents a higher gain since the input signal amplitude is lower, and its cutoff frequency should be over 10 Hz.

The main contributions of this study are: (1) The LNA presents an embedded tunable bandwidth (BW) with the use of a varactors' system controlled by external voltages that enables BW to range from 13.5 Hz to 3 kHz. It also presents embedded pseudo-resistors that enable the gain's tuning and is also controlled by an external voltage. This method can provide a gain range from 31 dB to 50 dB; (2) the LNA was conceptualized to accommodate the EMG and EOG biopotential signals, presenting two working modes, one with lower gain and higher BW for the EMG signal, and one higher gain and lower BW for the EOG; (3) the LNA was designed for noise minimization, consuming only 1.2 μW (including a self-biased current reference) while achieving competitive noise efficiency factor (NEF) and power efficiency factor (PEF) values; and (4) the circuit was fabricated and experimentally tested, showing the following specifications for the HCF mode: a gain of around 34.7 dB, a bandwidth (BW) of 1412 Hz, and an input referred noise of 1.407 μV , resulting in a NEF of 1.44 and PEF of 2.5, well on par with current state-of-the-art. The LCF's experimental measures show: a 39.5 dB gain with a 22.4 Hz BW, input referred noise of 0.829 μV , and

matching the NEF and PEF of 6.37 and 48.75, respectively. Both modes consume a current of 1 μA and present a total harmonic distortion (THD) under 1%.

The rest of this paper is organized as follows. Section 2 discusses related work. Section 3 explains the proposed LNA topology. In Section 4, simulation results are shown, presenting the circuits tuning capability; the experimental results are shown in Section 5; and finally, in Section 6, conclusions are drawn.

2. Related Work

State-of-the-art LNAs for biopotential signal acquisition are typically composed of operational transconductance amplifiers (OTAs) presenting a fully differential capacitive feedback structure [5,6,8–15]. This structure provides the LNA with a band-pass response where its mid-band gain can be easily set by the ratio between the input and feedback capacitors. Due to the input capacitors, this feedback structure is a noiseless form of attenuating the dc offset from the electrodes. Moreover, by opting for a fully differential topology, it helps to achieve a high common-mode rejection ratio (CMRR) and power supply rejection ratio (PSRR) [8]. Some work further introduces the feedback loop pseudo-resistors for better control in settling the LNA's BW [5,6,8–10,13,14,16] or even provides BW tunability [8]. Another development carried out on the capacitive feedback loop was the introduction of reset switches to initialize or reset the input and output standard mode voltages before the amplifier starts or when it is saturated [16,17]. An improvement over the conventional capacitive feedback is the T-network capacitive structure [4,18]. It has the advantage of reducing the sensitivity to mismatch and process variations by using larger capacitors with a small equivalent capacitance so that the input capacitor may be smaller.

LNAs are usually divided into two groups, the ones for signal detection and the ones for signal recording. The first group is characterized by presenting very low power consumption but higher noise values [6,8,9]. These LNAs are usually formed by simpler OTA topologies with a capacitive feedback structure to reduce the voltage supply and present a band-pass response. On the contrary, the latter target the acquisition of the signal in a truthful data stream, leading to LNAs showing higher power consumption and lower noise values [10–12,19]. These LNAs have more complex OTA topologies using techniques such as inverter-based input stages to reduce the noise and increase the transconductance under a given current, biasing the transistor in the sub-threshold region, use chopper modulation, and even stacking OTAs or input stages for current reuse to reduce their power consumption while maintaining a low noise level [4,10,11,13,14]. In Reference [10], a driving circuit is embedded in the inverter-based input stage to stabilize the current at the output stage, thus maximizing the current efficiency. Others, such as [13] or [14], use this technique for multi-channel applications. The first presents two folded-cascode amplifiers sharing a mid-rail current sink/source and current source, whereas the second explores a binary tree structure with several input differential pairs across multiple stages. This amplifier requires an output recombination stage that generates the output voltage by summing the output currents. Reference [11] also uses the current reuse technique on a folded-cascode amplifier. However, its focus is controlling the noise level on different channels by providing more power to the ones where the signal is detected.

To further reduce the noise levels, other LNAs use chopper modulation techniques [9,11–13,15,20]. By implementing choppers, the $1/f$ noise and dc offset are attenuated. However, its implementation has drawbacks since the choppers produce ripple and present limited input impedance, which must be mitigated with additional circuitry. The most common way to increase the input impedance is by using an impedance boosting loop [9] or a positive feedback loop [12,18]. An innovative form was developed in [20], which uses an input sampling input stage and digital–analog hybrid dc servo loop. As for chopping ripple suppression, it usually used a ripple reduction loop [12,20]; alternatively, a strategy can be the implementation of an auto-zero offset cancelation loop [18].

From these works, it can be seen that the LNAs can be more flexible since different biopotential signals have different characteristics in terms of voltage and bandwidth. By

using tunable pseudo-resistors and tunable varactors the proposed LNA can present specifications of each intended biopotential signal. Moreover, the tunability is implemented while maintaining a very competitive noise result and power efficiency.

Before moving on, it is also important to introduce two important performance figures for LNAs. A key figure when comparing LNAs is the NEF. It was first introduced in [21] and relates the input noise levels to the current consumption. It is expressed as:

$$\text{NEF} = V_{rms,in} \sqrt{\frac{2 \cdot I_{tot}}{\pi \cdot U_T \cdot 4 \cdot k \cdot T \cdot BW}} \quad (1)$$

where I_{tot} is the total current consumed, U_T is the thermal voltage, k is the Boltzmann constant, T is the temperature, and BW is the bandwidth. Later, in [22], the authors introduced the PEF, which is formulated as:

$$\text{PEF} = \text{NEF}^2 \cdot V_{DD}, \quad (2)$$

for improved comparison between LNAs with multiple power supplies.

3. Topology Description

The topology presented in this paper is based on the fully differential inverter-based current-mode IA from [19], with additional embedded tunable gain and tunable BW, as shown in Figure 2. It was first presented in [23], however, only at the post-layout level and developed in a 130 nm node. In this topology the tunable cutoff frequency is done with a varactor system that includes a bank of varactors for each cutoff frequency, being turned on and off according to the desired mode. The cutoff frequencies are set with an external control voltage ($VCTRL$) and two external control voltages (VH and VL) that turn the modes on and off. The embedded tunable gain is implemented by replacing R_2 with pseudo-resistors (P_2) also controlled by the same external voltage ($VCTRL$) that controls the cutoff frequency. This enables each mode to have its specific gain and cutoff frequency; however, in general, for a different application, the circuit may have different control voltages to tune the gain and BW independently.

The current-mode IA is a differential input–output amplifier with an inverter input stage (N1 and P1). The inverter, as the input stage, is used to reduce the noise level at this stage by doubling the transconductance under a given current. Plus, the gm/id is higher when biased in the sub-threshold region. Moreover, it is possible to reduce the input-referred noise (IRN) further if the inverter transistors at the input stage have a large area [10] since it reduces the flicker noise, which is the main type of noise contributor in these types of applications. The transistor N2 acts as a common-mode feedback loop, as it sets the current at the input as well as the common mode at the output of this stage. In the second stage, there is a transimpedance amplifier (N3), which sets the output gain with the resistor R_1 and the pseudo-resistors P_2 . The amplifier's gain is attained from the LNA's small-signal equivalent circuit presented in Figure 3 and follows the following expression:

$$\frac{V_O}{V_i} = \frac{R_2(g_{m_p}(R_1 - 2g_{m_3} \cdot r_{o_3} \cdot r_{o_n}) \cdot r_{o_p} - g_{m_n} \cdot r_{o_n}(R_1 + 2g_{m_3} \cdot r_{o_3} \cdot r_{o_p} + g_{m_p} \cdot R_1(r_{o_3} + g_{m_p} \cdot r_{o_3} \cdot r_{o_p}))}{2(R_2 + 2r_{o_3} + g_{m_3} \cdot R_2 \cdot r_{o_3})(r_{o_n} + r_{o_p}) + R_1 \cdot R_2(1 + g_{m_3} \cdot r_{o_3})(1 + g_{m_p} \cdot r_{o_p}) + \alpha_1}, \quad (3)$$

where α_1 is defined by:

$$\alpha_1 = 2R_1(r_{o_n} + r_{o_p} + r_{o_3}(1 + g_{m_3} \cdot r_{o_n}(1 + g_{m_p} \cdot r_{o_p}))). \quad (4)$$

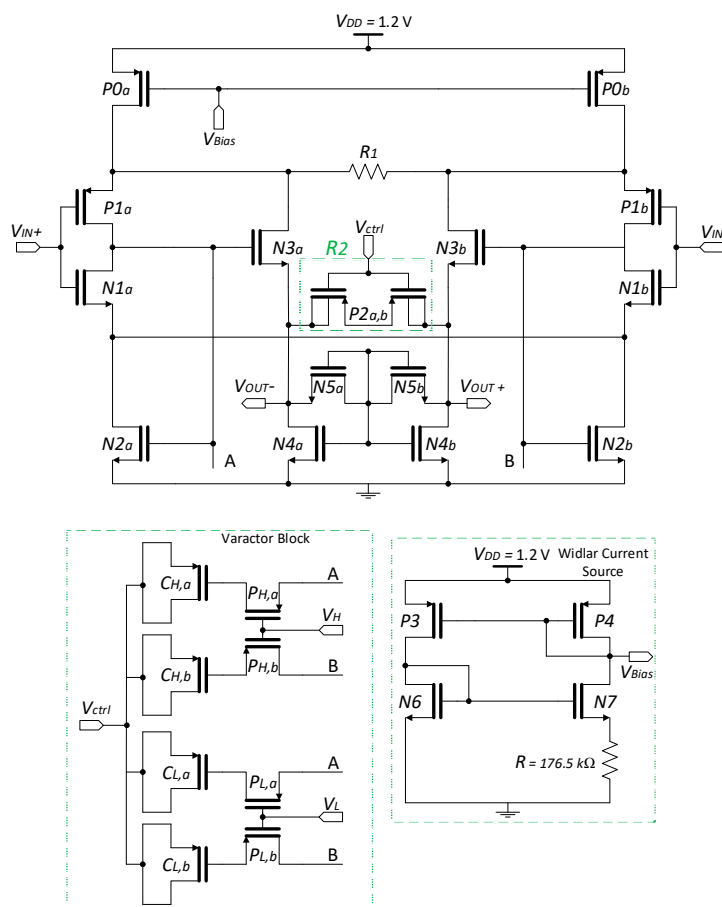


Figure 2. Proposed tunable LNA.

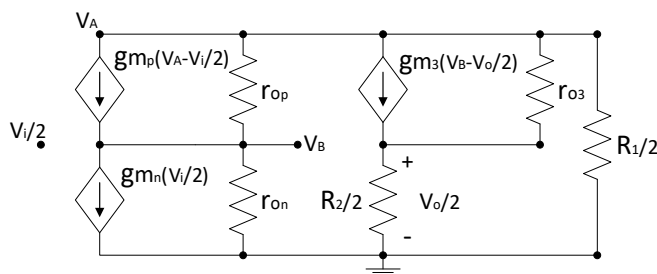


Figure 3. LNA's small-signal equivalent circuit.

Although in [19], it is mentioned that the gain, with some approximations and considerations, can be expressed as:

$$\frac{V_O}{V_i} = -\frac{R_2}{R_1}. \tag{5}$$

In this case, these mentioned approximations are not possible due to the much smaller current budget, although one may conclude that the ratio $P2/R1$ is proportional to the gain, meaning that if the ratio increases, the gain also increases. Other considerations about these two components are that the resistor $R1$ is directly linked to the noise performance, whereas the pseudo-resistors $P2$ are linked to the linearity. Both the noise and linearity increase with the increase in the respective component. Thus, adjusting the gain by tuning the $P2/R1$ ratio is easy. However, a trade-off between linearity and noise has to be considered. The circuit has more pseudo-resistors, the $N4$ devices that sense the common mode at the output stage. Therefore, along with $N5$, they operate as a common-mode feedback loop and define the current at this stage.

A varactor system for the cutoff frequency tuning is implemented between the first and second stages. The tunable varactor system is implemented with two pairs of varactors, one for each mode. The one respective to HCF was designed for a cutoff frequency for the EMG signal around 2000 Hz, and the one respective to LCF for a cutoff frequency over 20 Hz for the EOG signal. The varactors are a transistor with a structure that creates a capacitance effect with a small drawback in terms of area or noise introduction. In this work, the varactors have a D=S=B structure, meaning the drain, source, and bulk are connected. This connection establishes a capacitance with the gate (V_{BG}), with the capacitance being tuned according to the voltage at the D=S=B port. It was chosen since it is the only structure that works in multiple regions [24]. The total varactor capacitance can be given by $C_{CMOS} = C \cdot S$, where C is the capacitance per unit of area and S is the transistors channel area [25]. The maximum capacitance per unit can only be achieved in strong inversion (if the bulk-gate voltage is much higher than the threshold voltage, $V_{BG} \gg V_T$) or accumulation (if the bulk voltage is lower than the gate voltage, $V_B < V_G$) regions [26]. After each varactor, there is another transistor working as a switch to turn it on or off. This switch is controlled by external control voltages VH (for the HCF varactors) and VL (for the LCF varactors).

The pseudo-resistors (P2) are implemented using PMOS with a configuration consisting of the bulk connected to its drain, as shown in Figure 4. Due to the dependency of the threshold voltage on the substrate potential, this method results in a finite large equivalent resistance instead of an almost infinite impedance [27]. The pseudo-resistors can work in the cutoff region, presenting high resistance values in the giga-ohm order or, in the triode region, with lower resistances values of kilo-ohms [28], with the tuning being done by the external control voltage. The tuning feature enables different gains for each signal since they also present different amplitudes. When $VCTRL = 1.2$ V, the gain is higher than when $VCTRL$ is 0 V. The control code is $VCTRL = 0$ V, $VH = 0$ V, and $VL = 1.2$ V for the HCF mode, and $VCTRL = 1.2$ V, $VH = 1.2$ V, and $VL = 0$ V for the LCF mode.

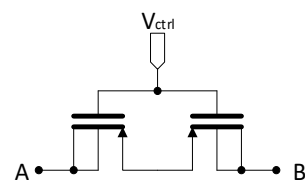


Figure 4. Pseudo-resistors configuration.

The fabricated circuit also includes a self-biased Widlar current reference for the LNA biasing, as in Figure 2. The current reference consumes 0.25 μ A from the 1 μ A current budget used in total.

4. Simulation Results

The fabricated sizing is shown in Table 2. The full layout is shown in Figure 5 and occupies an area of 0.624 mm² (964.66 μ m \times 647.47 μ m), with pads included. A major part of its area is occupied by a large bank of varactors that establish a low cutoff frequency of around 20 Hz.

Table 2. Fabricated device's sizing.

Device	w (μ m)	l (μ m)	Device	w (μ m)	l (μ m)
P0	285	20	N4	1	10
P1	78	50	N5	0.42	48.5
P2	3.5	43	PL	1	20
N1	192	50	PH	1	20
N2	0.41	50	CH	96	34
N3	55	30	CL	111	50

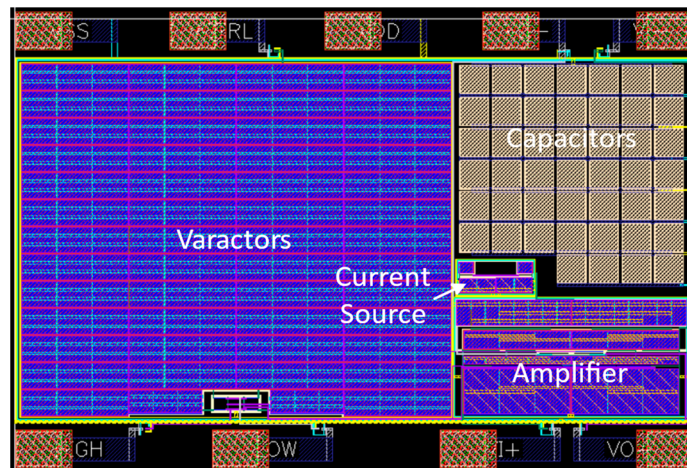


Figure 5. LNA's layout.

The simulation results from the post-layout analysis are summarized in Table 3. Figures 6 and 7 show the post-layout simulated results, where a gain of 34.8 dB with a BW of 2.06 kHz is expected for the HCF mode; as for the LCF mode, the simulated gain is 40 dB, and the BW is 20.5 Hz. The IRN for the HCF is 1.61 μV matching a NEF of 1.37 and a PEF of 2.24, whereas, for the LCF mode, the IRN is 0.407 μV , with a NEF of 3.46, and 14.36, respectively.

Table 3. Summary of the LNA's simulated and experimental results.

Results	Simulated		Experimental	
	HCF	LCF	HCF	LCF
Power (μW)	1.2	1.2	1.2	1.2
Gain (dB)	34.8	40	34.7	39.5
BW (Hz)	2062	20.5	1412	22.4
IRN (μV)	1.61	0.407	1.407	0.829
NEF	1.37	3.46	1.44	6.37
PEF	2.24	14.36	2.5	48.75
CMRR (dB)	>88.9	>78.8	>56.7	>58.9
PSRR (dB)	>98	>90	>79	>75.7
THD (%)	0.92	<0.01	0.68	0.46

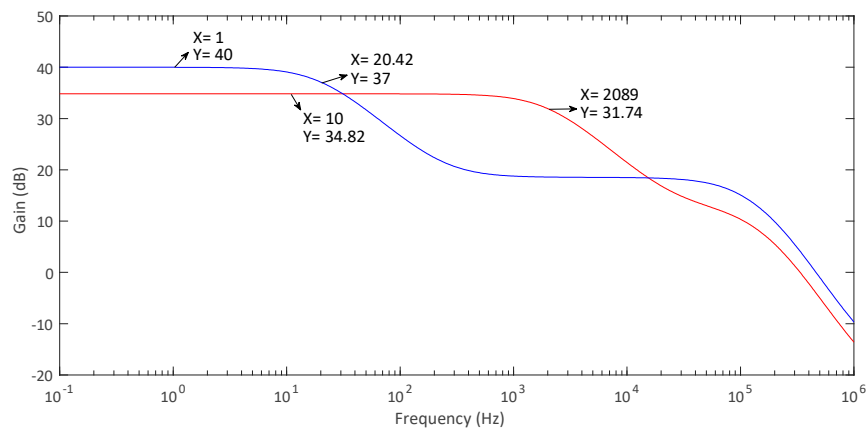


Figure 6. Simulated ac response of both HCF (red) and LCF (blue).

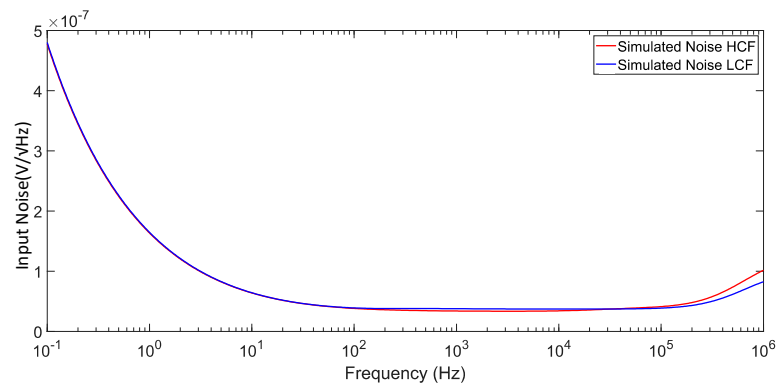


Figure 7. Simulated noise response of both HCF (red) and LCF (blue).

The LNA shows good linearity in comparison to state-of-the-art works with a THD under 1% for both modes. The CMRR and PSRR simulated values were obtained from a 500-run Monte-Carlo $\sigma = 3$ simulation, considering process and mismatch variations, and the results were obtained from the minimum value in the respective BW; therefore, the HCF presents a CMRR mean value of 88.9 dB with a standard deviation of 6.7 and the LCF a mean value of 78.8 dB with a standard deviation 8.3, as seen in Figure 8. In Figure 9, the PSRR histograms are illustrated for both the HCF and LCF obtained the same way as the CMRR previously, and the HCF case has a mean value of 98 dB with a 5 dB standard deviation, whereas the LCF presents a PSRR mean value of 90 dB and 5.2 standard deviation.

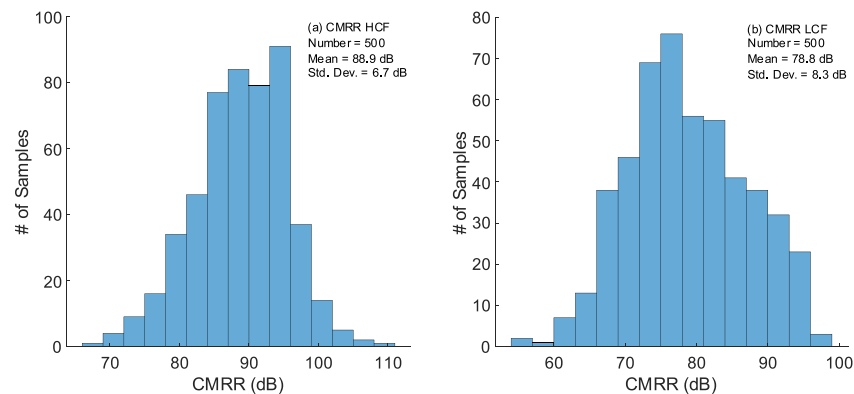


Figure 8. CMRR's variation with Monte-Carlo process and mismatch 500 runs: (a) HCF; (b) LCF.

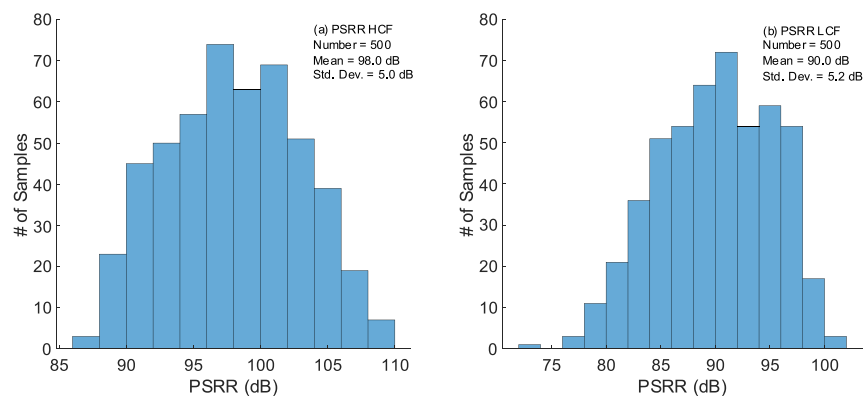


Figure 9. PSRR's variation with Monte-Carlo process and mismatch 500 runs: (a) HCF; (b) LCF.

To consider the circuit's variability in process and mismatch in regard to the other metrics, a 500-run Monte-Carlo $\sigma = 3$ simulation was performed. From the results shown

in Figures 10–12 concerning the HCF mode the gain, BW, and IRN present mean values of 34.7 dB, 2.1 kHz, and 1.6 μV with standard deviations of 0.8 dB, 313.5 Hz, and 78 nV, respectively. Regarding the LCF, mode gain has a mean value of 40 dB with a standard deviation of 1.3 dB, the BW shows a mean value of 20.9 Hz with a standard deviation of 3.6 Hz and the IRN presents a mean value of 330.3 nV with a standard deviation of 12.1 nV. From these results, one may conclude that the circuit has low variability, especially in terms of the input noise. It is also important to note that while gain and bandwidth have a larger variation they can be tuned after fabrication.

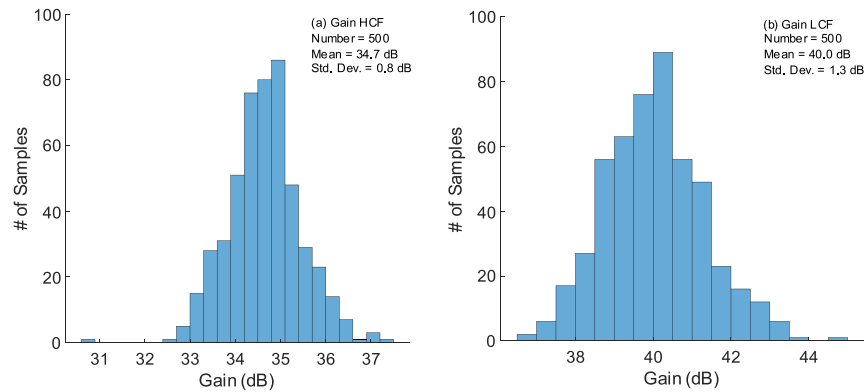


Figure 10. Gain’s variation with Monte-Carlo process and mismatch 500 runs: (a) HCF; (b) LCF.

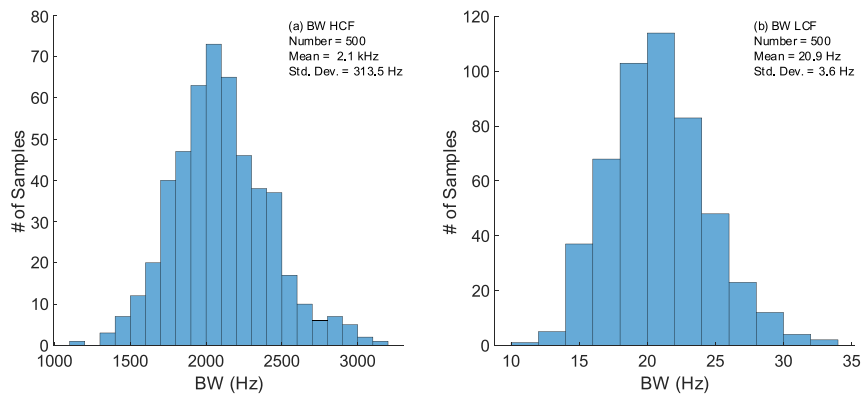


Figure 11. BW’s variation with Monte-Carlo process and mismatch 500 runs: (a) HCF; (b) LCF.

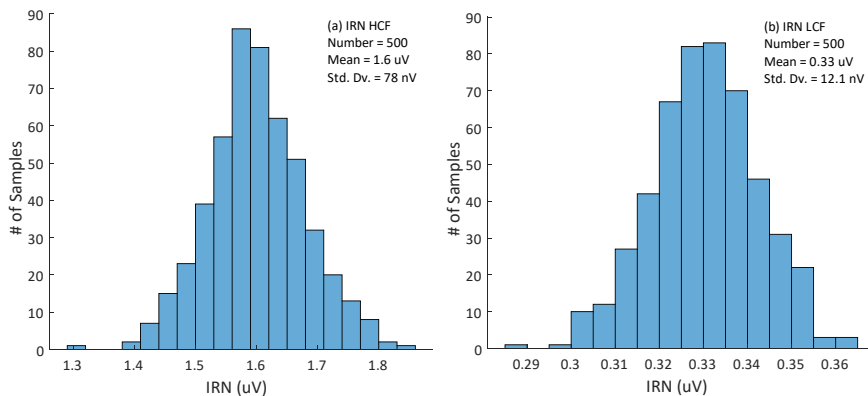


Figure 12. IRN’s variation with Monte-Carlo process and mismatch 500 runs: (a) HCF; (b) LCF.

Although when manufactured the LNA had the same V_{CTRL} connected to the pseudo-resistors (P2) and the varactors to tune the gain and BW, respectively, for other applications, it may be separated, thus having a control voltage to tune the gain and a different one to

tune the BW. To check the potential gain and BW ranges, the LNA was simulated with one control voltage to set the gain and another one to set the BW. First, the gain range in both modes, the varactors' control voltage is set to 0 V so that it has the same BW as in the HCF mode, and to 1.2 V to set the LCF's BW. The results obtained are shown in Figures 13 and 14, respectively. From Figure 13 one may perceive that as expected the gain increases until $VCTRL$ reaches around 0.4 V and stabilizes from then on, presenting a tuning range from 34.7 to 51.1 dB. Figure 14 shows that the gain decreases with the decrease in $VCTRL$ achieving a value of 30.8 dB.

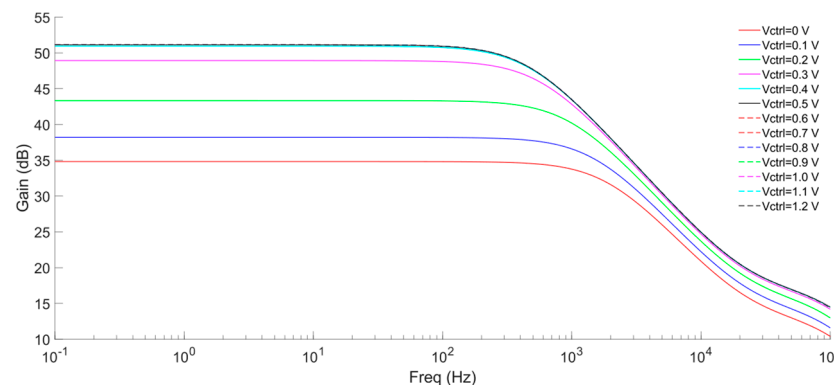


Figure 13. Illustration of the tuning gain capability for the HCF mode.

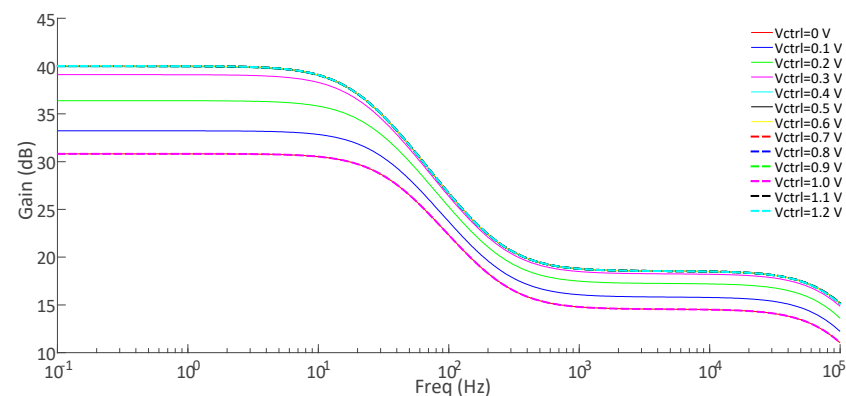


Figure 14. Illustration of the tuning gain capability for the LCF mode.

The BW's tuning range is analyzed in Figures 15 and 16; for these simulations, $P2$'s voltage control is set with 0 V and 1.2 V, respectively, as in the HCF and LCF modes. In Figure 15 the BW ranges from 0.851 kHz to 3 kHz, whereas in Figure 16 the BW ranges from 13.5 Hz to 24 Hz when the gain at 1 Hz is similar (0.1 dB variation), from $VCTRL = 0.9$ V to $VCTRL = 1.2$ V the BW's control voltage begins to influence the low-frequency gain.

For a better understanding of the circuit, it is also interesting to see the resistance values that pseudo-resistors $P2$ can achieve with the variation of $VCTRL$. This simulation was made by applying a square wave at the circuit's input and obtaining the output voltage and the current between the pseudo-resistors when the signal was high and low. In both cases, the pseudo-resistor had very identical values. In Figure 17 is perceived that the pseudo-resistors have a very high resistance variation, particularly from 0.4 V to 0.9 V. The resistance value of $P2$ varies from 4.36 M Ω to 2.38 T Ω .

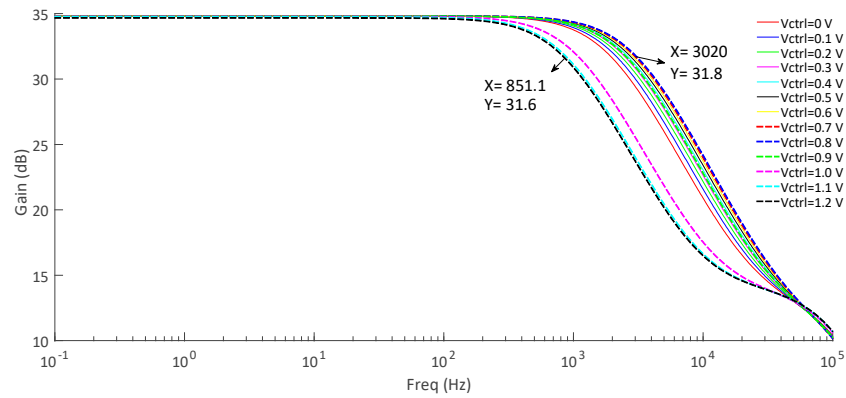


Figure 15. Tuning BW capability for HCF mode.

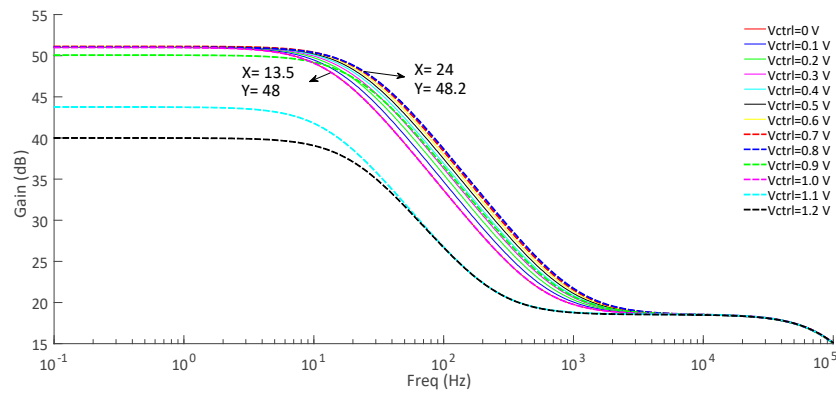


Figure 16. Tuning BW capability for LCF mode.

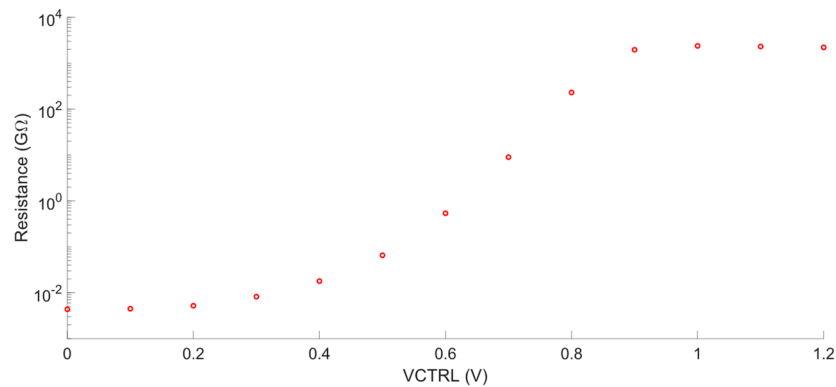


Figure 17. Variation of P2's resistance with V_{CTRL} .

5. Experimental Results

The proposed low-power LNA was fabricated in 110 nm UMC technology and wire-bonded to the printed circuit board (PCB) shown in Figure 18a; in Figure 18b a photograph of the die is shown. For measurement, and since the LNA presents differential input and output, its outputs were applied to a pre-amplifier (SRS SIM910 JFET Preamp) with unitary gain set for most measures, to convert it from differential to single-ended.

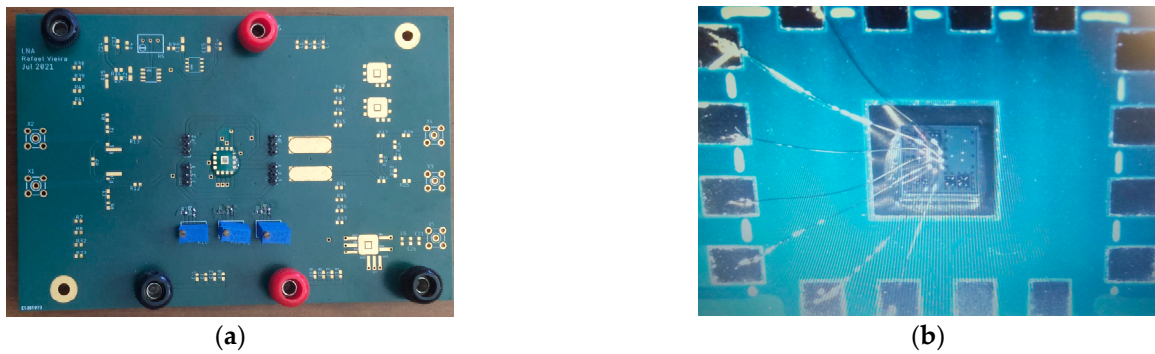


Figure 18. (a) Experimental test PCB with the die wire-bonded; (b) die photograph wire-bonded.

The measured current consumption is 1 μ A without the PCB’s extra circuitry. The measured LNA’s dc output was 492 mV with a deviation under 3 mV while presenting an input impedance of 7.48 M Ω . The LNA’s ac responses for both modes were measured using Analog Discovery 2 and are shown in Figure 19. It depicts an HCF gain of 34.7 dB and a BW of 1412 Hz, an LCF gain of 39.5 dB, and a BW of 22.4 Hz. To measure the signal’s linearity after amplification, a 1.85 mV and 120 Hz sinusoidal signal was set at the input of the amplifier in HCF mode. The resultant fast Fourier transform (FFT) is in Figure 20, where a THD of 0.68% is obtained. In the LCF mode, the input signal was 630 μ V with a frequency of 8 Hz. The THD achieved was 0.46%, and its FFT is in Figure 21.

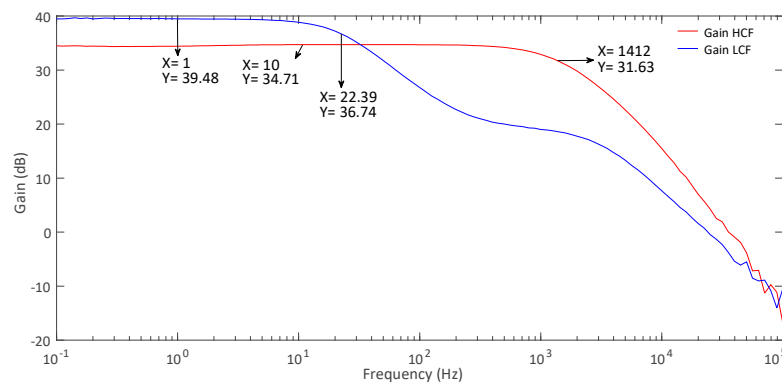


Figure 19. Measured ac response: HCF (red); LCF (blue).

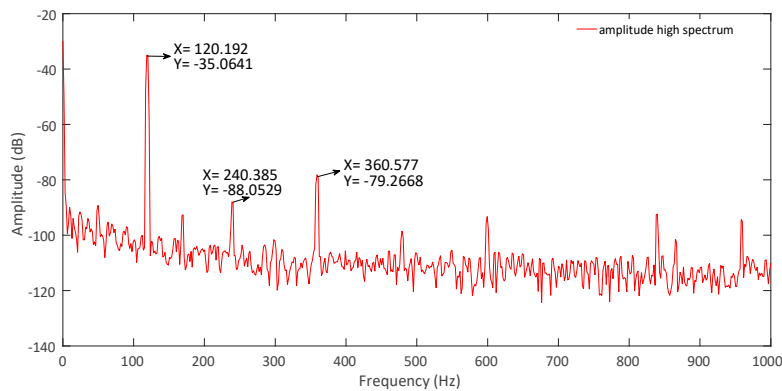


Figure 20. Measured HCF output signal spectrum.

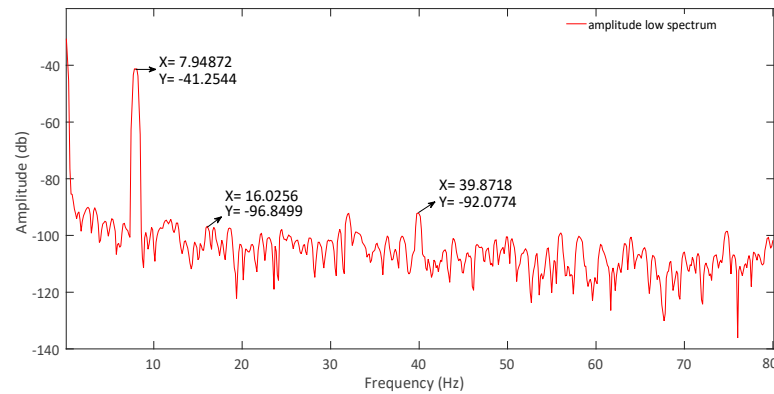


Figure 21. Measured LCF output signal spectrum.

The measured input noise voltage spectral density of both modes is shown in Figures 22 and 23. The noise measurements were done with the common mode applied to the LNA. For this measurement, the preamplifier’s gain was set to 50 to amplify the LNA’s noise above the noise floor of the baseband signal analyzer. The noise measurement had to be done from 1 Hz since the minimum BW resolution of the baseband signal analyzer is 0.5 Hz. In addition to the measured noise from the LNA, the noise from the preamplifier and baseband signal analyzer was also measured to remove their interference from the measured noise. In Figures 22 and 23, the 50 Hz line interference can be observed since it was not attenuated by any extra circuit, the influence is considerable, yet it was not removed for the noise calculations. Thus, integrating the input noise voltage spectral density from 1 Hz to each mode BW, 1412 Hz (HCF) and 22.4 Hz (LCF), an IRN of 1.407 μV , a NEF of 1.44 and a PEF of 2.5 is calculated for the HCF mode. In the LCF mode, the IRN is 0.829 μV , corresponding to a NEF and PEF of 6.37 and 48.75, respectively.

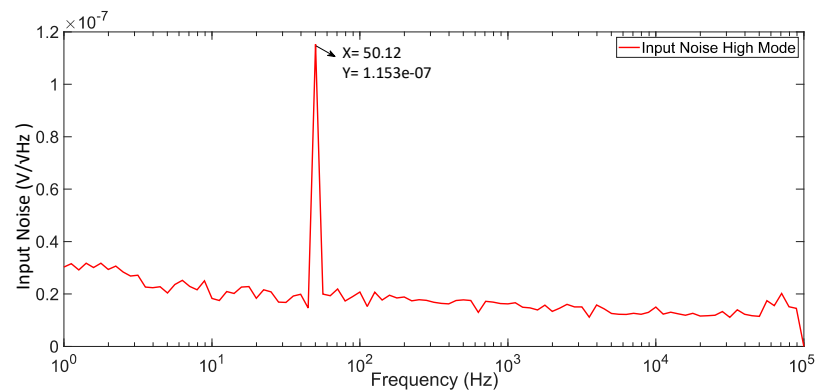


Figure 22. Measured HCF’s input noise response.

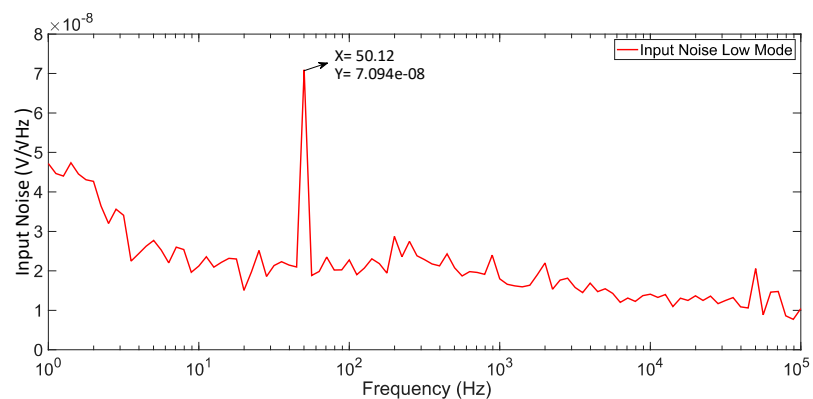


Figure 23. Measured LCF’s input noise response.

The CMRR and PSRR measures were also obtained using Analog Discovery 2. The PSRR and CMRR results are shown in Figures 24 and 25, depicting values of minimum values in their BW of 79 dB and 56.7 dB for HCF, whereas for LCF, the measures show values of 75.7 dB and 58.9 dB, respectively. These values are without considering the 50 Hz interference, which has a significant influence, especially in the PSRR measures. The discrepancies between the simulated and measured results are mainly seen under 4 Hz, especially in the LCF mode in terms of noise, which is likely to be introduced by the varactors. The BW is another metric that has a high variance between the simulated and experimental results, this occurs due to the input impedance of the preamplifier and Analog Discovery 2 which were not considered in post-layout simulations.

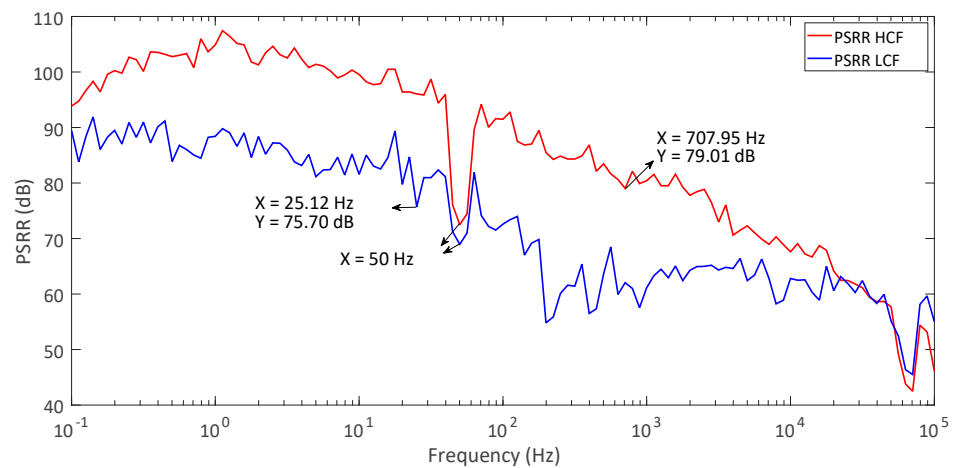


Figure 24. Measured PSRR: HCF (red); LCF (blue).

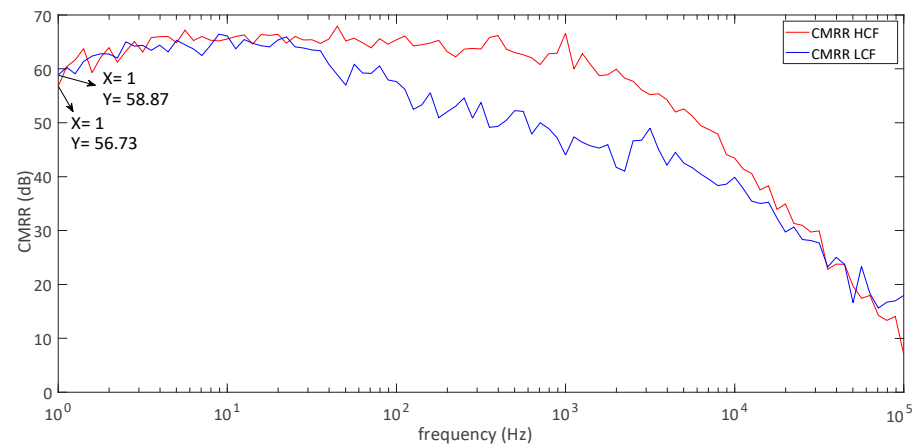


Figure 25. Measured CMRR: HCF (red); LCF (blue).

The summarized experimental results, along with other state-of-the-art LNAs in the recent bibliography, are presented in Table 4. This work achieves the desired tunability with bandwidths of 20 Hz and 1.4 kHz for gains of 34 dB and 39.5 dB. While consuming only 1 μ A, very competitive noise results are achieved, namely, HCF's mode IRN, NEF, and PEF 1.407 μ V, 1.44, and 2.5, respectively, with the NEF being the lowest measured among the state-of-the-art.

Table 4. Comparison of the LNA's simulated results and state-of-the-art works.

Results	[4]	[10]	[11]	[19]	[18] *	[29] *	[30] *	[31]	This Work	
									HCF	LCF
Year	2018	2018	2015	2015	2022	2020	2022	2021	2023	
Tech. (nm)	180	350	180	180	180	180	180	500	110	
Area (mm ²)	0.072	0.18	1.6 #	0.096	0.09	0.046	-	0.046	0.624	
Gain (dB)	35	39.8	33	40	40	39.2	39.9	49.3/60.5	34.7	39.5
BW (Hz)	9.3 k	0.2–200	0.7–182	11 k	800	3–5 k	0.4–10.3 k	0.5–301/ 270–12.9 k	1412	22.4
IRN (μV)	3.6	2.05	0.34/1	0.78	1.8	3.03	1.2/3.3	3.16	1.407	0.829
NEF	1.94	2.26	1.74/2	1.88	5.4	2.4	3/1.2	2.53	1.44	6.37
PEF	6.77	10.2	1.1/2.5	6.36	29.7d	8.06	16.6/2.7	21.1	2.5	48.75
Supply (V)	1.8	2	1.2	1.8	1.0	1.4	1	3.3	1.2	
Power (μW)	4.5	0.32	1.2/0.3	78.84	1.21	2.98	1.7	4.12	1.2	
CMRR (dB)	76	>65	>70	100	>108	>70	68.6	97.1	>56.7	>58.9
PSRR (dB)	80	>70	>70	-	87	>77	73.3	84.4	>79	>75.7
THD (%)	0.07	<1	1.5	-	-	1	0.82	0.68	0.68	0.46
	@1 mV	@15 mV	@2.3 mV	-	-	@13 mV	@1 mV	-	@1.8 mV	@0.6 mV

* Simulated results. # Includes extra circuitry.

6. Conclusions

This paper presents a low-power LNA based on a current mode instrumentation amplifier, with tunable gain and tunable BW, controlled from an external source, with two main working modes for biopotential signals, the EMG and EOG. The reconfigurability features are provided using tunable pseudo-resistors for the gain, and a tunable varactor system for the BW, controlled with an external voltage. Although the circuit was fabricated using only one control voltage for the tuning of both the gain and the BW, if a control voltage is implemented for each, the circuit can achieve a maximum tuning gain of around 16 dB and a maximum BW tuning of 2.17 kHz on the HCF mode. The LNA was manufactured using the UMC 110 nm design kit, and experimental results show gains of 34.7 dB and 39.5 dB for the HCF and LCF modes, respectively. With its 1 μA consumption and IRN of 1.44 μV rms noise, it achieves very competitive noise performance.

Author Contributions: Conceptualization, R.V. and R.P.; analytic analysis and design, R.V.; layout R.V. and R.P.; experimental measurements, R.V.; methodology, R.V. and R.P.; validation, R.V., R.P. and F.N.; resources and laboratory equipment, F.N. and N.L.; writing—original draft preparation, R.V.; writing—review and editing, R.V., N.L., R.M. and F.N.; supervision, N.H., N.L. and R.P.; project administration, N.L. All authors have read and agreed to the published version of the manuscript.

Funding: This research was funded by Fundação para a Ciência e a Tecnologia—Ministério da Ciência, Tecnologia e Ensino Superior (FCT/MCTES) through national funds and, when applicable, co-funded by European Union (EU) funds under the project UIDB/50008/2020, including internal research projects HAICAS (X-0009-LX-20) and Grant SRH/BD/07774/2021.

Data Availability Statement: Data available on request due to restrictions.

Conflicts of Interest: The authors declare no conflict of interest.

References

- Movassaghi, S.; Abolhasan, M.; Lipman, J.; Smith, D.; Jamalipour, A. Wireless Body Area Networks: A Survey. *IEEE Commun. Surv. Tutor.* **2014**, *16*, 1658–1686. [[CrossRef](#)]
- Jani, A.B.; Bagree, R.; Roy, A.K. Design of a Low-Power, Low-Cost ECG & EMG Sensor for Wearable Biometric and Medical Application. In Proceedings of the 2017 IEEE SENSORS, Glasgow, UK, 29 October–1 November 2017.
- Thakor, N. Biopotentials and Electrophysiology Measurement. In *Telehealth and Mobile Health*, 1st ed.; CRC Press: Boca Raton, FL, USA, 2015; pp. 555–574.
- Rezaei, M.; Maghsoudloo, E.; Bories, C.; De Koninck, Y.; Gosselin, B. A Low-Power Current-Reuse Analog Front-End for High-Density Neural Recording Implants. *IEEE Trans. Biomed. Circuits Syst.* **2018**, *12*, 271–280. [[CrossRef](#)] [[PubMed](#)]

5. Lo, Z.-J.; Nath, B.; Wang, Y.-C.; Huang, Y.-J.; Huang, H.-C.; Peng, S.-Y. A Floating-Gate-Based Four-Channel Reconfigurable Analog Front-End Integrated Circuit. In Proceedings of the 2021 IEEE International Symposium on Circuits and Systems (ISCAS), Daegu, Republic of Korea, 22–28 May 2021.
6. Bose, S.; Shen, B.; Johnston, M.L. A Batteryless Motion-Adaptive Heartbeat Detection System-on-Chip Powered by Human Body Heat. *IEEE J. Solid-State Circuits* **2020**, *55*, 2902–2913. [[CrossRef](#)] [[PubMed](#)]
7. Vieira, R.; Passos, F.; Martins, R.; Horta, N.; Lourenço, N. Behavioral Analysis of Noise and Bandwidth Specifications of Heartbeat Detection Circuits for Ultra Low Power Devices. *IEEE Access* **2023**, *11*, 27330–27341. [[CrossRef](#)]
8. Kosari, A.; Breiholz, J.; Liu, N.; Calhoun, B.; Wentzloff, D. A 0.5 V 68 nW ECG Monitoring Analog Front-End for Arrhythmia Diagnosis. *J. Low Power Electron. Appl.* **2018**, *8*, 27. [[CrossRef](#)]
9. Chen, Y.; Jeon, D.; Lee, Y.; Kim, Y.; Foo, Z.; Lee, I.; Langhals, N.B.; Kruger, G.; Oral, H.; Berenfeld, O.; et al. An InjecTable 64 nW ECG Mixed-Signal SoC in 65 nm for Arrhythmia Monitoring. *IEEE J. Solid-State Circuits* **2015**, *50*, 375–390. [[CrossRef](#)]
10. Zhang, J.; Zhang, H.; Sun, Q.; Zhang, R. A Low-Noise, Low-Power Amplifier with Current-Reused OTA for ECG Recordings. *IEEE Trans. Biomed. Circuits Syst.* **2018**, *12*, 700–708. [[CrossRef](#)] [[PubMed](#)]
11. Song, S.; Rooijackers, M.; Harpe, P.; Rabotti, C.; Mischi, M.; van Roermund, A.H.M.; Cantatore, E. A Low-Voltage Chopper-Stabilized Amplifier for Fetal ECG Monitoring With a 1.41 Power Efficiency Factor. *IEEE Trans. Biomed. Circuits Syst.* **2015**, *9*, 237–247. [[CrossRef](#)] [[PubMed](#)]
12. Fan, Q.; Sebastiano, F.; Huijsing, J.H.; Makinwa, K.A.A. A 1.8 μ W 60 nV/ $\sqrt{\text{Hz}}$ Capacitively-Coupled Chopper Instrumentation Amplifier in 65 nm CMOS for Wireless Sensor Nodes. *IEEE J. Solid-State Circuits* **2011**, *46*, 1534–1543.
13. Song, S.; Rooijackers, M.; Harpe, P.; Rabotti, C.; Mischi, M.; van Roermund, A.H.M.; Cantatore, E. A Multiple-Channel Frontend System with Current Reuse for Fetal Monitoring Applications. In Proceedings of the 2014 IEEE International Symposium on Circuits and Systems (ISCAS), Melbourne, Australia, 1–5 June 2014.
14. Sepehrian, H.; Mirbozorgi, S.A.; Gosselin, B. A Low-Power Current-Reuse Analog Front-End for Multi-Channel Neural Signal Recording. In Proceedings of the 2014 IEEE 12th International New Circuits and Systems Conference (NEWCAS), Trois-Rivieres, QC, Canada, 22–25 June 2014.
15. Yaul, F.M.; Chandrakasan, A.P. A Noise-Efficient 36 nV/ $\sqrt{\text{Hz}}$ Chopper Amplifier Using an Inverter-Based 0.2-V Supply Input Stage. *IEEE J. Solid-State Circuits* **2017**, *52*, 3032–3042. [[CrossRef](#)]
16. Zhang, X.; Zhang, Z.; Li, Y.; Liu, C.; Guo, Y.X.; Lian, Y. A 2.89 μ W Dry-Electrode Enabled Clockless Wireless ECG SoC for Wearable Applications. *IEEE J. Solid-State Circuits* **2016**, *51*, 2287–2298. [[CrossRef](#)]
17. Harrison, R.R. The Design of Integrated Circuits to Observe Brain Activity. *Proc. IEEE* **2008**, *96*, 1203–1216. [[CrossRef](#)]
18. Pham, X.T.; Vu, T.K.; Nguyen, T.D.; Pham-Nguyen, L. A 1.2- μ W 41-dB Ripple Attenuation Chopper Amplifier Using Auto-Zero Offset Cancellation Loop for Area-Efficient Biopotential Sensing. *Electronics* **2022**, *11*, 1149. [[CrossRef](#)]
19. Das, D.; Srivastava, A.; Ananthapadmanabhan, J.; Ahmad, M.; Baghini, M.S. A Novel Low-Noise Fully Differential CMOS Instrumentation Amplifier with 1.88 Noise Efficiency Factor for Biomedical and Sensor Applications. *Microelectron. J.* **2016**, *53*, 35–44. [[CrossRef](#)]
20. Xu, W.; Wang, T.; Wei, X.; Yue, H.; Wei, B.; Duan, J.; Li, H. Low Noise, High Input Impedance Digital-Analog Hybrid Offset Suppression Amplifier for Wearable Dry Electrode ECG Monitoring. *Electronics* **2020**, *9*, 165. [[CrossRef](#)]
21. Steyaert, M.S.J.; Sansen, W.M.C. A Micropower Low-Noise Monolithic Instrumentation Amplifier for Medical Purposes. *IEEE J. Solid-State Circuits* **1987**, *22*, 1163–1168. [[CrossRef](#)]
22. Muller, R.; Gambini, S.; Rabaey, J.M. A 0.013 mm² 5 μ W DC-Coupled Neural Signal Acquisition IC with 0.5 V Supply. In Proceedings of the 2011 IEEE International Solid-State Circuits Conference, San Francisco, CA, USA, 20–24 February 2011.
23. Vieira, R.; Martins, R.; Horta, N.; Lourenço, N.; Póvoa, R. A Sub-1 μ A Low-Power Low-Noise Amplifier with Tunable Gain and Bandwidth for EMG and EOG Biopotential Signals. In Proceedings of the Conference on PhD Research in Microelectronics and Electronics (PRIME), Erfurt, Germany, 19–22 July 2021.
24. Sameni, P.; Siu, C.; Mirabbasi, S.; Djahanshahi, H.; Hamour, M.; Iniewski, K.; Chana, J. Modeling and Characterization of VCOs with MOS Varactors for RF Transceivers. *EURASIP J. Wirel. Commun. Netw.* **2006**, *2006*, 32. [[CrossRef](#)]
25. Li, S.; Zhang, T. Simulation and Realization of MOS Varactors. *Procedia Eng.* **2012**, *29*, 1645–1650. [[CrossRef](#)]
26. Andreani, P.; Mattisson, S. On the use of MOS Varactors in RF VCOs. *IEEE J. Solid-State Circuits* **2000**, *35*, 905–910. [[CrossRef](#)]
27. Tajalli, A.; Leblebici, Y.; Brauer, E. Implementing Ultra-High-Value Floating Tunable CMOS Resistors. *Electron. Lett.* **2008**, *44*, 349–350. [[CrossRef](#)]
28. Tajalli, A.; Vittoz, E.; Leblebici, Y.; Brauer, E.J. Ultra Low Power Subthreshold MOS Current Mode Logic Circuits Using a Novel Load Device Concept. In Proceedings of the 33rd European Solid-State Circuits Conference (ESSCIRC), Munich, Germany, 11–13 September 2007.
29. Naderi, K.; Shad, E.; Molinas, M.; Heidari, A. A Power Efficient Low-noise and High Swing CMOS Amplifier for Neural Recording Applications. In Proceedings of the 42nd Annual International Conference of the IEEE Engineering in Medicine & Biology Society (EMBC), Montreal, QC, Canada, 20–24 July 2020.

30. Mohtasham-Nia, M.-A.; Yavari, M. A Low-Power Low-Noise Neural Recording Amplifier with Improved Telescopic-Cascode OTA. In Proceedings of the 2021 Iranian International Conference on Microelectronics (IICM), Tehran, Iran, 22–24 December 2021.
31. Tasneem, N.T.; Mahbub, I. A 2.53 NEF 8-bit 10 kS/s 0.5 μm CMOS Neural Recording Read-Out Circuit with High Linearity for Neuromodulation Implants. *Electronics* **2021**, *10*, 590. [[CrossRef](#)]

Disclaimer/Publisher's Note: The statements, opinions and data contained in all publications are solely those of the individual author(s) and contributor(s) and not of MDPI and/or the editor(s). MDPI and/or the editor(s) disclaim responsibility for any injury to people or property resulting from any ideas, methods, instructions or products referred to in the content.